AIAA SciTech Forum
January 3-7, 2022, San Diego, CA & Virtual
AIAA SCITECH 2022 Forum

10.2514/6.2022-0734

Hypersonic Boundary-Layer Instability on a Highly Cooled Cone. Part I: Q-FLDI Measurement and Instability Calculations

A. Hameed,* D. Shekhtman,† and N. J. Parziale‡
Stevens Institute of Technology, Hoboken, NJ 07030, USA.

L. Paquin,§ S. N. Skinner,¶ and S. J. Laurence‖
University of Maryland, College Park, MD 20742, USA

W. M. Yu** and J. M. Austin††
California Institute of Technology, Pasadena, CA 91125, USA

In this paper, a Q-FLDI system was constructed to correlate disturbances inside and outside of the boundary layer over a blunted cone in high-enthalpy, hypersonic flow at T5, the free-piston-driven reflected-shock tunnel at California Institute of Technology. We present results for three shots representing a fully-turbulent case with a 5 mm nose-tip radius, an unstable case with a 5 mm nose-tip radius at moderate enthalpy (6 MJ/kg), and an unstable case with a 2 mm nose-tip radius at higher enthalpy (10.5 MJ/kg). In the fully-turbulent case, the spectra indicate the possibility of a region where there is a power-law variation in the spectrum. For the unstable case with a 2 mm nose-tip radius at higher enthalpy (10.5 MJ/kg), the FLDI detected the second mode instability at approximately 1 MHz. This agrees well with results obtained using the schlieren technique for experiments performed in this campaign at similar conditions. The mismatch when compared to stability calculations for this case could be attributed to run-condition calculation error. An unstable case with a 5 mm nose-tip radius at moderate enthalpy (6 MJ/kg) is also presented. In this case, there is more content measured outside of the boundary layer than inside. For this case, computations of the mean flow show that the entropy-layer had not been swallowed at the point of measurement suggesting the elevated energy content outside the boundary layer could be due to entropy layer instabilities or oblique waves not considered in the stability analysis.

I. Introduction

At the centerline of the blunted leading edge of a slender cone in hypersonic flow, gas passes through a nearly normal shock. However, further away from the centerline, the oblique shock becomes curved and the flow is processed by a shock with a shallower shock angle. As the entropy increase across a shock is proportional to the shock strength, the entropy increase at the leading edge is greater than the entropy increase away from the body centerline, creating an entropy gradient that flows downstream along the surface of the body. As the classical boundary layer grows, it eventually "swallows" the entropy layer. Rotta [1] notes that stability analysis of such a flow may be complicated, relative to a sharp cone, because "[t]he entropy layer caused by the curved shock associated with nose blunting provides a rotational external stream through which the boundary layer develops."

*Graduate Student, Mechanical Engineering, 1 Castle Point on Hudson, Hoboken, New Jersey, 07030, USA.
†Graduate Student, Mechanical Engineering, 1 Castle Point on Hudson, Hoboken, New Jersey, 07030, USA.
‡Associate Professor, Mechanical Engineering, 1 Castle Point on Hudson, Hoboken, New Jersey, 07030, Senior AIAA Member.
§Graduate Student, Aerospace Engineering, Department of Aerospace Engineering, College Park, Maryland, 20742. Student AIAA Member.
¶Postdoc, Aerospace Engineering, Department of Aerospace Engineering, College Park, Maryland, 20742. Student AIAA Member.
‖Associate Professor, Aerospace Engineering, Department of Aerospace Engineering, College Park, Maryland, 20742. Senior AIAA Member.
**PhD Candidate, Graduate Aerospace Laboratories, 1200 E. California Blvd, MC 105-50.
††Professor of Aerospace, Graduate Aerospace Laboratories, 1200 E. California Blvd, MC 105-50, Associate Fellow AIAA

The design of hypersonic vehicles is highly dependent on determining the point of boundary layer transition. Transition from a laminar to a turbulent boundary layer can increase surface heating loads by a factor of 4-10 [2], increasing the cooling requirements and therefore the weight of the thermal protection system. The inability to reliably predict the transition location leads to a conservative design of the hypersonic vehicle.

The study of hypersonic flow is made difficult by the high velocities, stagnation temperatures, and broad ranges of length and time scales characteristic of this flow regime. These unique features present limitations for traditional flow-diagnostic techniques. For example, hot-wire anemometers are encumbered by wire breakage, limited frequency response, flow intrusion, and signal interpretation problems and heat-flux gauges and pressure transducers have limited bandwidth and are restricted to on-surface measurements. With recent improvements in imaging, electronics, and laser technology, non-intrusive optical diagnostic techniques have gained popularity [3–5].

Focused laser differential interferometry (FLDI) is a novel nonparticle-based optical flow diagnostic technique pioneered by Smeets[6–11] and Smeets and George[12] in the 1970s. From the 1980s to the 2000s, other researchers have used laser differential interferometry (LDI) to make measurements in high-speed flows.[13–18] More recently, Parziale et al.[19–25] used the FLDI technique to characterize the facility disturbance level and boundary-layer instability and transition in the Caltech T5 reflected-shock tunnel. Additional advancements to the technique have been made since that time allowing for the reliable measurement of convective velocity between two closely spaced FLDI probe volumes,[26–33] facility disturbance-level characterization[34–36], and novel beam shaping techniques for application in hard-to-access flows.[37–41] Additionally, researchers have devised controlled problems[42–44] to test the data-reduction strategies developed by Fulghum[45], Settles and Fulghum[46], Schmidt and Shepherd[47], and Hameed and Parziale[57].

II. Facility and Experimental Setup

A. T5 Reflected-Shock Tunnel

The experiments in this campaign were performed at T5, the free-piston-driven reflected-shock tunnel at California Institute of Technology. This facility is designed to simulate high-enthalpy, real gas effects on the aerodynamics of vehicles flying at hypervelocity speeds through the atmosphere. Additional information regarding the capabilities of T5 can be found in Hornung [48].

In T5, a 120 kg aluminum piston is loaded into the compression tube/secondary reservoir junction. A 127 μm thick Mylar secondary diaphragm is inserted at the nozzle throat and a 7-10 mm thick stainless steel primary diaphragm is inserted between the compression tube and the shock tube. After the facility is evacuated, the shock tube is filled with the test gas (for these experiments, ALPHAGAZ air), the compression tube is filled with a He/Air mixture, and the secondary reservoir is pressurized with air. The air in the secondary reservoir is released, launching the piston into the compression tube. The driver gas in the compression tube is adiabatically compressed by the piston until the primary diaphragm ruptures. The rupture of the primary diaphragm causes a shock wave to propagate in the shock tube. The shock wave reflects off the end wall, bursts the secondary diaphragm, and re-processes the test gas to high temperature and pressure with negligible velocity. The test gas is then expanded through a convering-diverging contoured nozzle to a hypersonic Mach number in the test section.

The freestream run conditions are determined from the nozzle reservoir conditions. To first determine the reservoir conditions, the shock tube pressure, P_1, and the measured incident shock speed, U_s, are used to evaluate the thermodynamic state of the test gas in the nozzle reservoir. It is assumed that this state isentropically expands to the reservoir pressure, P_R, accounting for weak expansion or compression waves that are reflected between the contact surface and the shock tube end wall. These calculations are performed using Cantera [49], with the Shock and Detonation Toolbox[50]. The calculated reservoir conditions are inputted into the University of Minnesota Nozzle Code to determine the freestream conditions once the gas has been steadily expanded through the contoured nozzle [51–54]. The reservoir and freestream run conditions for all of the shots performed thus far in this experimental campaign are presented in Table 1 and Table 2. The freestream conditions are chosen to be an areal average of the DPLR output at 700±10 mm from the throat because this was the location of the nose tip.

A blunted 5-degree half-angle cone was used as the model in this experimental campaign. Two cone nose-tip bluntnesses were used in these experiments, one with a 5 mm radius and another with a 2 mm radius. The cone was placed at zero angle of attack in the center of the test section.

Table 1 Reservoir Conditions

Shot	Gas	P_R	h_R	T_R	ρ_R	y_{N_2}	y_{O_2}	y_{NO}	y_N	y_O	R_N	Diag
		(MPa)	(MJ/kg)	(K)	(kg/m^3)	(-)	(-)	(-)	(-)	(-)	(mm)	(-)
2947	Air	53.8	9.33	5901	28.8	0.700	0.057	0.137	0.004	0.103	5	FLDI
2948	Air	59.2	8.60	5616	33.9	0.699	0.073	0.141	0.002	0.085	5	FLDI
2949	Air	58.5	7.39	5096	37.9	0.702	0.102	0.139	0.001	0.057	5	FLDI
2950	Air	30.2	4.51	3654	28.5	0.729	0.180	0.082	0.000	0.009	5	FLDI
2951	Air	38.9	3.89	3298	40.8	0.738	0.196	0.062	0.000	0.003	5	FLDI
2952	Air	36.0	4.17	3467	35.8	0.734	0.189	0.072	0.000	0.006	5	FLDI
2953	Air	29.3	4.80	3810	26.4	0.725	0.172	0.090	0.000	0.013	5	FLDI
2954	Air	28.6	5.49	4152	23.4	0.718	0.152	0.106	0.000	0.024	5	FLDI
2955	Air	26.0	6.35	4533	19.2	0.711	0.125	0.119	0.000	0.044	5	FLDI
2956	Air	60.0	9.05	5811	32.9	0.699	0.064	0.140	0.003	0.095	2	FLDI
2957	Air	57.2	10.45	6378	27.8	0.699	0.039	0.129	0.008	0.125	2	FLDI
2958	Air	58.3	10.22	6289	28.8	0.699	0.043	0.132	0.007	0.120	2	Schlieren
2959	Air	57.8	9.76	6099	29.7	0.699	0.050	0.135	0.005	0.111	2	Schlieren
2960	Air	57.5	9.90	6154	29.3	0.699	0.048	0.134	0.006	0.114	2	Schlieren
2961	Air	58.5	9.78	6108	30.1	0.699	0.050	0.135	0.005	0.111	2	Schlieren
2962	Air	58.7	9.31	5915	31.5	0.699	0.058	0.138	0.004	0.101	2	Schlieren
2963	Air	60.6	9.30	5915	32.5	0.698	0.059	0.139	0.004	0.100	2	Schlieren
2964	Air	58.5	9.60	6035	30.6	0.699	0.053	0.137	0.005	0.107	2	FLDI

B. FLDI Setup

To develop the Q-FLDI setup used in this experimental campaign, a linearly polarized laser beam was first expanded using a diverging lens. The expanding beam was then split into 1 row of 6 "spots" using a Holo/Or MS-474-Q-Y-A diffractive optic [55, 56]. The position and orientation of this diffractive optic set the streamwise interspacing of the FLDI beams. Another Holo/Or diffractive optic (DS-192-Q-Y-A) was used to make an additional row of the already split beams. This diffractive optic set the wall-normal interspacing of the FLDI beams. The 2 rows and 6 columns of beams generated by the diffractive optic were sent through a quarter-wave plate before being split once more by a 2-arcminute Wollaston prism to generate the intraspaced beam pairs in the FLDI setup. The beam pairs were then focused on top of the center of the cone using a converging lens of appropriate focal length. A second Wollaston prism of equal separation angle and a linear polarizer was used to recombine the intraspaced beams. Four of the twelve "spots" generated by the diffractive optics were selected to be directed onto photodetectors. The interference of the intraspaced beam pairs was measured by a change in intensity measured by the photodetector. Fig. 1 shows the positioning of the components used to generate the Q-FLDI setup.

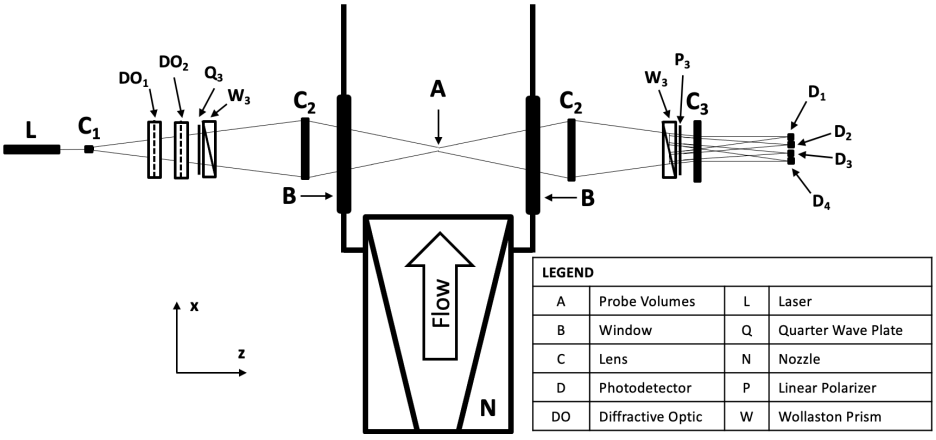

Fig. 1 Components used to generate Q-FLDI setup in this experimental campaign. The diffractive optics generated a 2 row by 6 column grid of beams. The Wollaston prism generated the orthogonally polarized intraspaced beam pairs, four of which were recombined and focused onto individual photodetectors.

Table 2 Freestream Conditions

Shot	U_X	ρ_X	P_X	T_X	Tv_X	M_X	Re_X^U	y_{N_2}	y_{O_2}	y_{NO}	y_N	y_O
	(m/s)	(kg/m^3)	(kPa)	(K)	(K)	(-)	(1/m)	(-)	(-)	(-)	(-)	(-)
2947	3894	0.074	31.1	1436	1433	5.09	5.35e+06	0.733	0.184	0.073	0.000	0.010
2948	3772	0.085	31.6	1290	1285	5.21	6.31e+06	0.733	0.188	0.074	0.000	0.006
2949	3544	0.087	25.8	1029	1032	5.49	7.05e+06	0.731	0.189	0.078	0.000	0.002
2950	2844	0.055	8.1	508	610	6.28	5.77e+06	0.737	0.198	0.065	0.000	0.000
2951	2676	0.078	9.5	420	533	6.50	8.77e+06	0.741	0.203	0.057	0.000	0.000
2952	2756	0.069	9.1	459	563	6.41	7.47e+06	0.739	0.200	0.061	0.000	0.000
2953	2921	0.052	8.3	553	642	6.19	5.25e+06	0.735	0.196	0.069	0.000	0.001
2954	3101	0.048	9.4	672	731	5.96	4.56e+06	0.732	0.192	0.074	0.000	0.001
2955	3299	0.042	10.1	834	867	5.68	3.64e+06	0.731	0.188	0.078	0.000	0.003
2956	3858	0.085	34.1	1388	1383	5.13	6.17e+06	0.733	0.186	0.073	0.000	0.008
2957	4080	0.074	35.8	1648	1646	4.96	5.10e+06	0.733	0.178	0.073	0.000	0.016
2958	4045	0.077	35.9	1607	1605	4.99	5.30e+06	0.733	0.180	0.073	0.000	0.014
2959	3973	0.078	34.7	1524	1521	5.04	5.51e+06	0.733	0.183	0.073	0.000	0.011
2960	3994	0.077	34.8	1548	1545	5.02	5.40e+06	0.733	0.182	0.073	0.000	0.012
2961	3978	0.079	35.3	1528	1525	5.04	5.58e+06	0.733	0.183	0.073	0.000	0.011
2962	3904	0.082	34.4	1441	1438	5.09	5.90e+06	0.733	0.185	0.073	0.000	0.009
2963	3902	0.085	35.4	1438	1434	5.10	6.10e+06	0.733	0.186	0.073	0.000	0.009
2964	3950	0.080	35.0	1496	1493	5.06	5.70e+06	0.733	0.184	0.073	0.000	0.010

The beams were oriented such that the streamwise interspacing and intraspacing were parallel to the cone's surface and the wall-normal interspacing was perpendicular to the cone's surface. For these experiments, a wall-normal interspacing of 2.03 mm was achieved and a streamwise interspacing of 2.74 mm was selected. The lower set of beams were positioned approximately 600 µm above the cone's surface, within the 1 mm boundary layer that was estimated for these experiments. Given the wall-normal beam interspacing, this placed the second set of beams at roughly 2.6 mm. The beams were placed approximately 650 mm away from the tip of the 5 mm blunted cone and approximately 680 mm away from the tip of the 2 mm blunted cone.

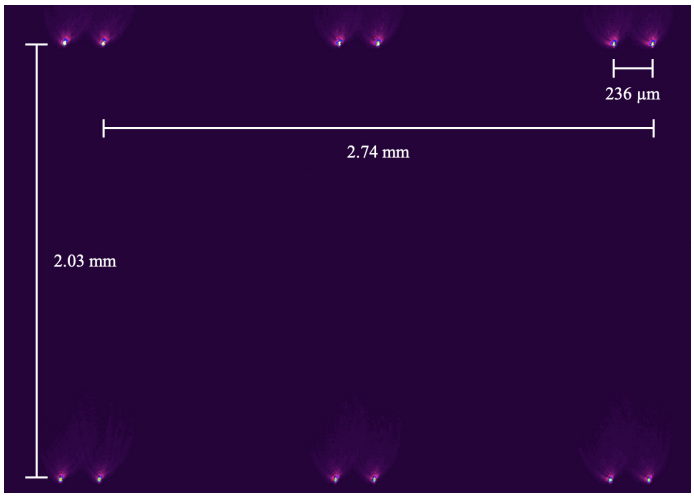

Fig. 2 Picture of Q-FLDI beam pairs taken at the focus above the cone using an Ophir-Spiricon LT665 beam profiling camera. The middle column of FLDI beam pairs were not chosen to be focused onto photodetectors as they did not allow all four beams to be centered on their respective fringes.

A picture showing the beam inter- and intraspacing is provided in Fig. 2. The positioning of the beams above the center of the cone is shown in Fig. 3.

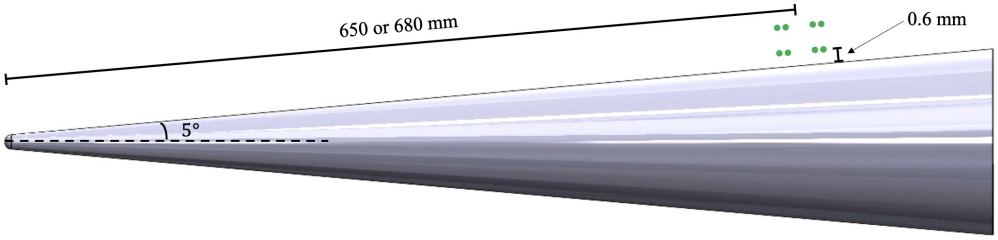

Fig. 3 Location of Q-FLDI beams relative to the 5 degree cone with blunt nose. Depending on the bluntness of the cone nosetip used for the experiment, the beams were located 650 mm or 680 mm along the cone. The wall normal position of the lower set of beams was adjusted to be approximately 0.6 mm above the cone surface. The wall normal position of the upper set of beams was set by the beam interspacing. The beams were oriented to be parallel to the cone's surface in the streamwise direction.

III. Results and Discussion

In this section, we present results for shots 2951, 2955, and 2957. These experiments represent a fully-turbulent case with a 5 mm nose-tip radius, an unstable case with a 5 mm nose-tip radius at moderate enthalpy (6 MJ/kg), and an unstable case with a 2 mm nose-tip radius at higher enthalpy (10.5 MJ/kg).

Shot 2951 is an example of a fully-turbulent experiment, evidenced by the broadband response shown in the associated spectrogram (Fig. 4a). We zoom in to 25 µs of test time to show the correlation between two closely-spaced FLDI probes at the same wall normal distance. Using MATLAB's `xcorr` function [27], we determine the peak lag between the signals occurs at approximately 1.43 µs, and using the measured streamwise beam interspacing, we approximate a convective velocity of 1916 m/s.

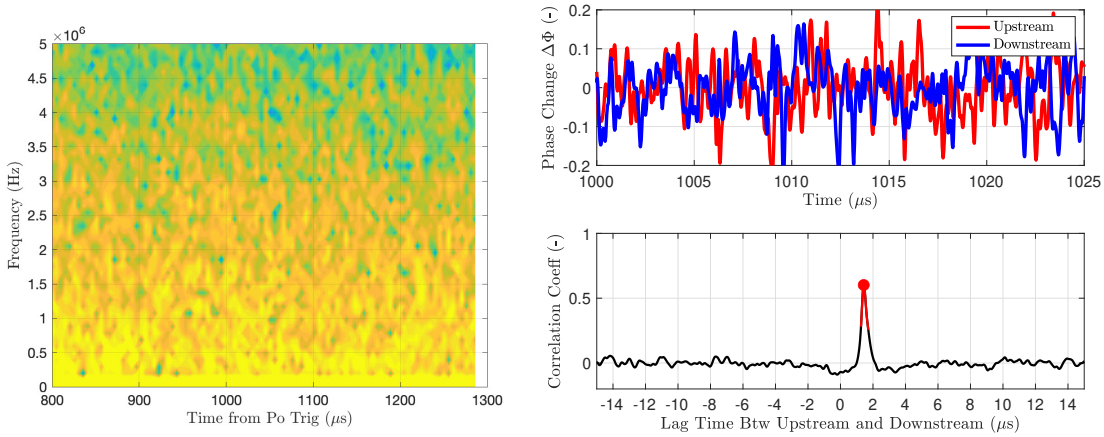

(a) (b)

Fig. 4 (a) Spectogram for shot 2951 showing broadband turbulent response as measured by an FLDI probe. (b) Cross correlation of two closely spaced FLDI probes for shot 2951 showing the measured phase change (top) and the maximum lag time between the signals (bottom).

The corrected PSDs of the disturbances measured by all four FLDI probes are presented in Fig.5. These PSDs are corrected only by the differencing effects between the interfering FLDI beams in a beam pair. As shown, all four FLDI probes exhibit a similar response and may have a power-law variation in the spectrum. Further analysis of the correction to the FLDI data is still required in this case.

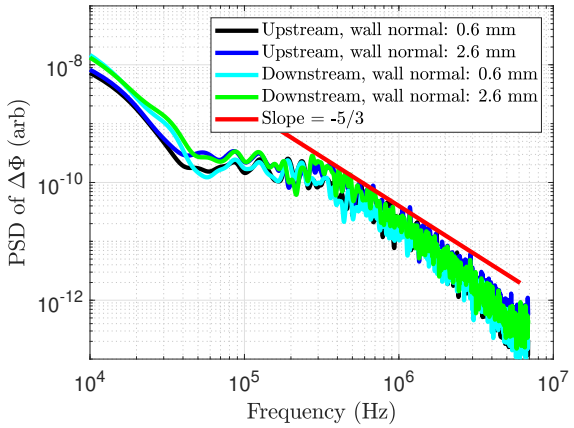

Fig. 5 Corrected PSDs of Shot 2951 showing turbulent response. PSDs are corrected only by incorporating the differencing effects of the FLDI instrument. All four FLDI probes exhibit a similar response.

Shot 2957 is an example of an experiment where the second-mode instability was measured. The spectrogram in Fig. 6a shows the second-mode instability being intermittently present during the test time. Corrected PSDs for the two

upstream FLDI probes at different wall normal distances are presented in Fig. 6b. These PSDs were corrected using the process detailed in Hameed and Parziale [57]. The transfer function representing a two-dimensional disturbance field occupying a discrete domain was used to correct the PSD. A convective velocity of 2884 m/s was calculated. The FLDI probe closer to the wall shows the second-mode instability occuring at approximately 1022 kHz. The sharp peaks at 1300 kHz and 1430 kHz are most likely local AM radio stations KAZN and KMRB, respectively. In the future, efforts will be made to mitigate this electrical noise. Stability calculations were made for this case with PSE-Chem, which is a part of the STABL software package described in Johnson et al.[53, 58]. The linear stability diagram for shot 2957 is presented in Fig. 6c. A vertical black line is placed in Fig. 6c, at a position 680 mm along the cone, representing the measurement location for this shot. The growth rate as calculated by STABL across the frequency range at this measurement location is presented in Fig. 6d and shows the most-amplified frequency to be approximately 1200 kHz. The width, and the shape at high frequencies, of the most amplified frequency at this condition is a unique feature, and could be indicative of a case where the supersonic mode would be present. This feature was not seen in Parziale et al. [25], which were experiments and STABL calculations performed at similar conditions in T5, but with a sharp cone. We also note that for this case, the maximum N factor was 11.5 with a peak disturbance frequency of approximately 1500 kHz, which is appreciably different from the experimental observation.

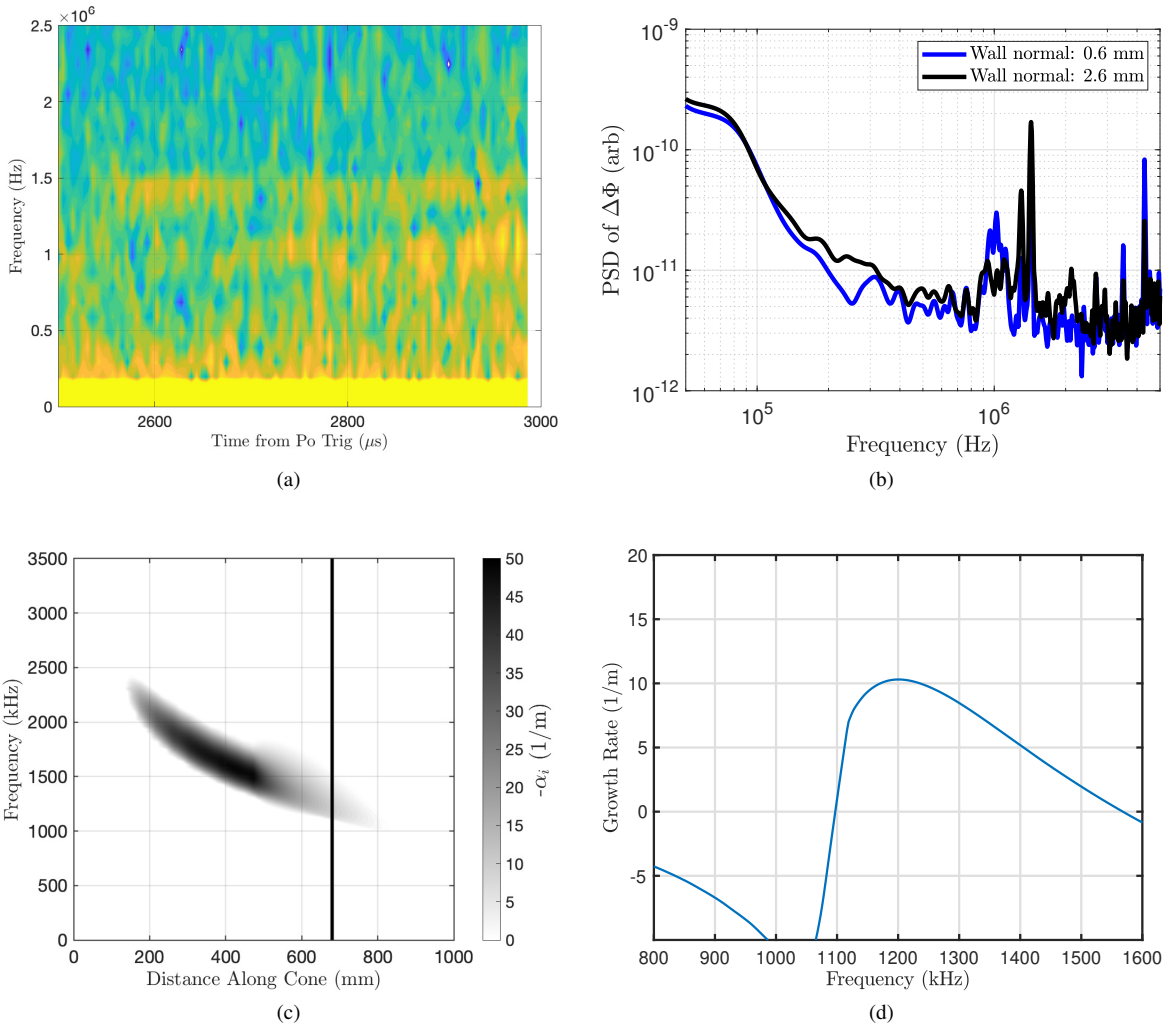

Fig. 6 (a) Spectrogram for shot 2957 showing some second-mode wave packets at about 1000 kHz. (b) Spectra showing measurement of second-mode. (c) Linear stability diagram for shot 2957. Vertical black line represents the measurement location, which is at 680 mm along the cone. (d) Growth rate at the measurement location denoted by the black line.

We next present results for shot 2955. As seen in the in the spectra for the four FLDI probes, the probes further away from the surface show different behavior than those close to the wall. Relative to the probes near the wall, there is more energy content over a relatively broad band as well as a narrow band peak at 580 kHz. We note that the boundary-layer thickness calculated by DPLR was 1.6 mm at this measurement location, meaning that the content at the wall normal position of 2.6 mm is outside of the boundary layer. Stability calculations were also performed for this case and appear in Fig. 7c and Fig. 7d. We note that the maximum N factor at the measurement location was 3.5 at 690 kHz. We note that in Fig. 7d, there does not appear to be an unstable region at high frequnecy as there was in Fig. 6d, likely because of the lower enthalpy (wall-temperature ratio) and lower Reynolds number. One potential explanation for the elevated disturbance content outside the boundary layer is the entropy layer.

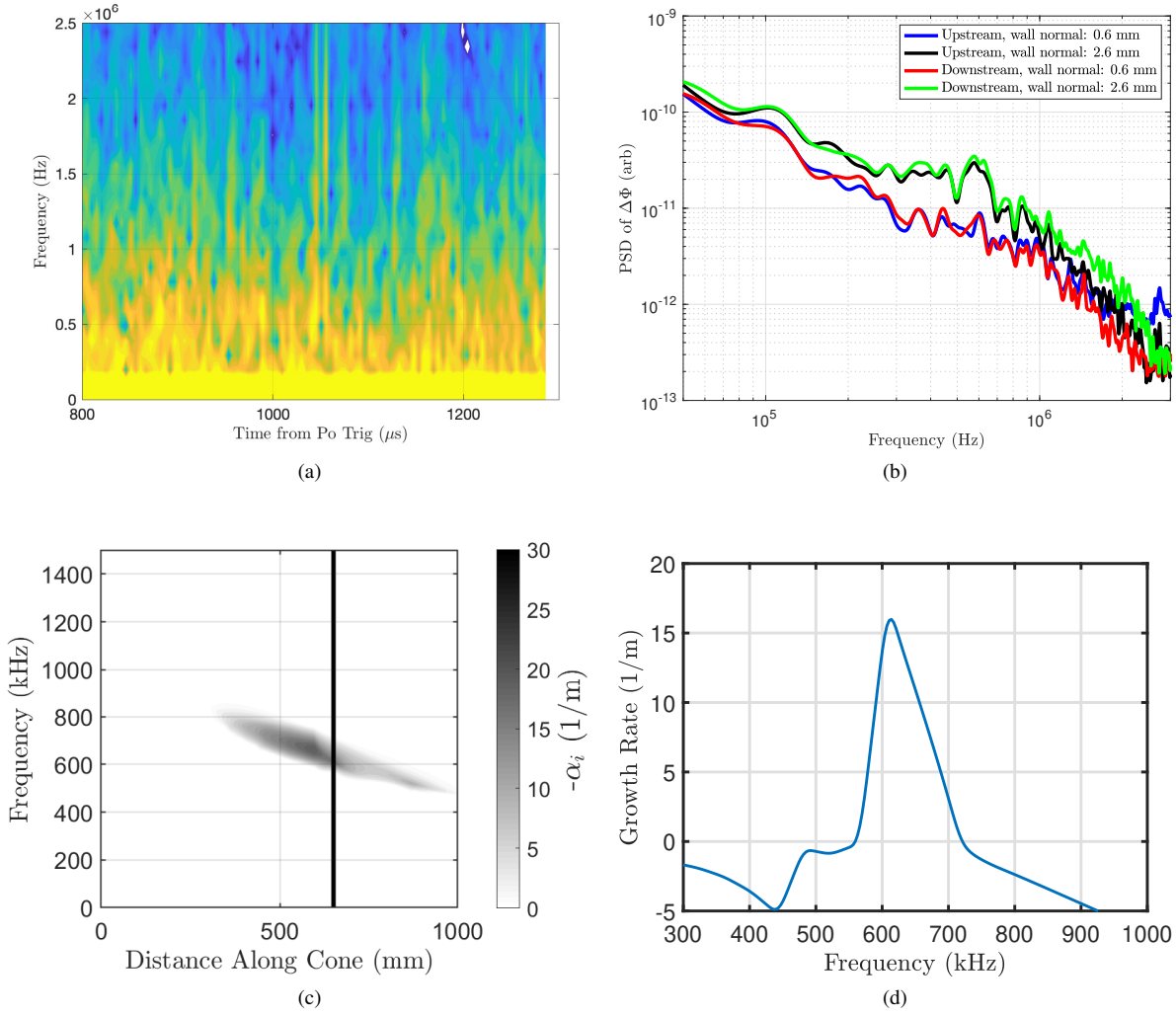

Fig. 7 (a) Spectrogram and (b) spectra for shot 2955. The spectrogram is for a downstream FLDI probe with a wall normal distance of 2.6 mm. The spectra shows content measured further away from the cone surface that is not present near the surface.

One way to identify where the effects of bluntness are important is to find the swallowing distance (X_S), or the distance where the boundary-layer thickness becomes larger than the entropy-layer thickness, and relate the swallowing distance to the location where the FLDI experiments were performed (X_T). To do this, we compute the entropy change in reference to the freestream as

$$ds = c_p \log(T/T_\infty) - R \log(P/P_\infty), \tag{1}$$

where c_p and R are the mass-specific heat at constant pressure and the gas constant, respectively. We define the entropy-

layer thickness as the wall-normal location where the mass-specific entropy increases above the post-normal-shock mass-specific entropy. In Fig. 8, we show the change in entropy per Eq. 1, the entropy-layer thickness as a dashed line, and the boundary-layer thickness as a solid line for shot 2955 and 2957. The swallowing distances for these two experiments were computed to be 745 mm and 120 mm, respectively (noting that the FLDI measurement location was at 650 mm for shot 2955 and 680 mm for shot 2957). That is, the entropy layer had still not been swallowed for the data in Fig. 7, whereas for the data in Fig. 6, the entropy layer had been swallowed 560 mm upstream (over 100 boundary-layer thicknesses). This elevated level of disturbance outside of the boundary layer could be oblique waves not considered in the stability calculations, or an entropy-layer instability.

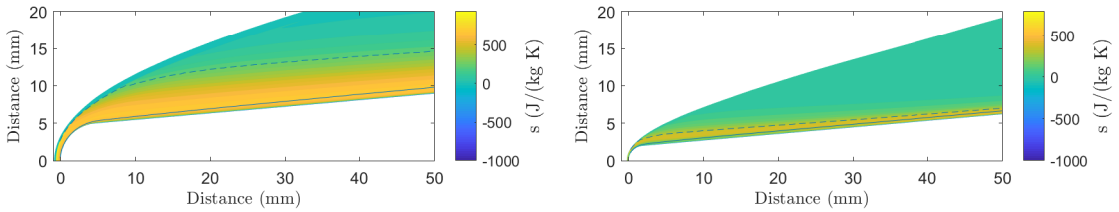

Fig. 8 Method for computing the entropy layer swallowing distance. Left is shot 2955, right is shot 2957. Entropy computed as change from freestream. Dashed line represents entropy layer, solid line is boundary-layer.

IV. Conclusions

In this paper, we constructed an Q-FLDI system intended to correlate disturbances inside and outside of the boundary layer over a blunted cone in high-enthalpy, hypersonic flow. We present results for shots 2951, 2955, and 2957. These experiments represent a fully-turbulent case with a 5 mm nose-tip radius, an unstable case with a 5 mm nose-tip radius at moderate enthalpy (6 MJ/kg), and an unstable case with a 2 mm nose-tip radius at higher enthalpy (10.5 MJ/kg). In the fully-turbulent case, the spectra indicate the possibility of a region where there is a power-law variation in the spectrum. Additional work reducing the FLDI signal will be required to make further assessment. For the unstable case with a 2 mm nose-tip radius at higher enthalpy (10.5 MJ/kg), the FLDI detected the second mode at approximately 1 MHz. This agrees well with the result measured by Paquin et al. using the schlieren technique for shots 2958 and 2959 [59]. The convective velocities and second-mode frequencies measured with the two methods differ by less than 5% for the three tests ranging Re = 5.1-5.5 $\times 10^6$ 1/m and h = 9.8-10.5 MJ/kg. However, the corresponding stability calcuations for shot 2957 predicted a max N factor at 1.5 MHz. This mismatch could be due to run-condition calculation error resulting in an incorrect calculation of the mean flow. However, researchers have performed experiments measuring the mean flow in T5 showing reasonable agreement between the measured and computed nozzle flow [60–62]. We also present an unstable case with a 5 mm nose-tip radius at moderate enthalpy (6 MJ/kg) where there is more content measured outside of the boundary layer than inside. We made computations of the mean flow to show that the entropy-layer thickness had not yet been swallowed in this case. Furthermore, two possible explanations for these disturbances outside the boundary layer include oblique waves not considered in the stability calculations or an entropy-layer instability.

Acknowledgments

Support for this work was provided by the Air Force Office of Scientific Research Grants FA9550-16-1-0262 and FA9550-18-1-0403. Additionally, there was support from Air Force Small Business Innovation Research contracts FA9101-17-P-0094 and FA2487-19-C-0013. The authors would also like to acknowledge the expertise of Bahram Valiferdowsi and Noel Esparza-Duran in operating the shock tunnel.

References

[1] Rotta, N. R., "Effects of Nose Bluntness on the Boundary Layer Characteristics of Conical Bodies at Hypersonic Speeds," AD-0645668 or NYU-AA-66-66, 1966.

[2] Bitter, N. P., and Shepherd, J. E., "Stability of highly cooled hypervelocity boundary layers," *Journal of Fluid Mechanics*, Vol. 778, No. 10, 2015, pp. 586–620. https://doi.org/10.1017/jfm.2015.358.

[3] Danehy, P. M., Weisberger, J., Johansen, C., Reese, D., Fahringer, T., Parziale, N. J., Dedic, C., Estevadeordal, J., and Cruden, B. A., "Non-Intrusive Measurement Techniques for Flow Characterization of Hypersonic Wind Tunnels," *Flow Characterization and Modeling of Hypersonic Wind Tunnels (NATO Science and Technology Organization Lecture Series STO-AVT 325)*, NF1676L-31725 - Von Karman Institute, Brussels, Belgium, 2018.

[4] Laurence, S. J., Wagner, A., Hannemann, K., Wartemann, V., Lüdeke, H., Tanno, H., and Itoh, K., "Time-Resolved Visualization of Instability Waves in a Hypersonic Boundary Layer," *AIAA Journal*, Vol. 50, No. 6, 2012, pp. 243–246. https://doi.org/10.2514/1.56987.

[5] Kennedy, R. E., Laurence, S. J., Smith, M. S., and Marineau, E. C., "Investigation of the second-mode instability at Mach 14 using calibrated schlieren," *Journal of Fluid Mechanics*, Vol. 845, 2018. https://doi.org/10.1017/jfm.2018.269.

[6] Smeets, G., and George, A., "Gas Dynamic Investigations in a Shock Tube using a Highly Sensitive Interferometer," Translation of isl internal report 14/71, Original 1971, Translation 1996.

[7] Smeets, G., "Laser Interferometer for High Sensitivity Measurements on Transient Phase Objects," *IEEE Transactions on Aerospace and Electronic Systems*, Vol. AES-8, No. 2, 1972, pp. 186–190. https://doi.org/10.1109/TAES.1972.309488.

[8] Smeets, G., and George, A., "Anwendungen des Laser-Differentialinterferometers in der Gasdynamik," ISL - N 28/73, Also translated by Goetz, A.: ADA-307459, 1973.

[9] Smeets, G., "Laser-Interferometer mit grossen, fokussierten Lichtbündeln für lokale Messungen," ISL - N 11/73, 1973.

[10] Smeets, G., "Verwendung eines Laser-Differentialinterferometers zur Bestimmung lokaler Schwankungsgrössen sowie des mittleren Dichteprofils in cinem turbulenten Freistrahl," ISL - N 20/74, 1974.

[11] Smeets, G., "Flow Diagnostics by Laser Interferometry," *IEEE Transactions on Aerospace and Electronic Systems*, Vol. AES-13, No. 2, 1977, pp. 82–90. https://doi.org/10.1109/TAES.1977.308441.

[12] Smeets, G., and George, A., "Laser Differential Interferometer Applications in Gas Dynamics," Translation of ISL Internal Report 28/73, Original 1975, Translation 1996.

[13] Azzazy, M., Modarress, D., and Hoeft, T., "High sensitivity Density Fluctuation Detector," *Proceedings of SPIE Vol. 569 High Speed Photography, Videography, and Photonics I/I*, SPIE, San Diego, CA, 1985. https://doi.org/10.1117/12.949865.

[14] Azzazy, M., Modarress, D., and Trolinger, J. D., "Feasibility Study of Optical Boundary Layer Transition Detection Method," NASA-CR-178109, 1986.

[15] Azzazy, M., Modarress, D., and Hoeft, T., "High-sensitivity Density Fluctuation Detector," *Journal of Physics E: Scientific Instruments*, Vol. 20, No. 4, 1987, p. 428. https://doi.org/10.1088/0022-3735/20/4/017.

[16] O'Hare, J. E., "A Nonperturbing Boundary-Layer Transition Detector," *Proceedings of SPIE 0569, High Speed Photography, Videography, and Photonics III*, San Diego, California, 1985, pp. 58–63. https://doi.org/10.1117/12.949864.

[17] Collicott, S. H., Schneider, S. P., and Messersmith, N. L., "Review Of Optical Diagnostic Methods For Hypersonic Low-Noise Facilities," *Proceedings of 34th Aerospace Sciences Meeting and Exhibit*, AIAA-96-0851, Reno, NV, 1996. https://doi.org/10.2514/6.1996-851.

[18] Salyer, T. R., Collicott, S. H., and Schneider, S. P., "Feedback Stabilized Laser Differential Interferometry for Supersonic Blunt Body Experiments," *Proceedings of 38th Aerospace Sciences Meeting and Exhibit*, AIAA-2000-0416, Reno, Nevada, 2000. https://doi.org/10.2514/6.2000-416.

[19] Parziale, N. J., Shepherd, J. E., and Hornung, H. G., "Reflected Shock Tunnel Noise Measurement by Focused Differential Interferometry," *Proceedings of 42nd AIAA Fluid Dynamics Conference and Exhibit*, AIAA-2012-3261, New Orleans, Louisiana, 2012. https://doi.org/10.2514/6.2012-3261.

[20] Parziale, N. J., Jewell, J. S., Shepherd, J. E., and Hornung, H. G., "Optical Detection of Transitional Phenomena on Slender Bodies in Hypervelocity Flow," *Proceedings of RTO Specialists Meeting AVT-200/RSM-030 on Hypersonic Laminar-Turbulent Transition*, NATO, San Diego, California, 2012.

[21] Parziale, N. J., Shepherd, J. E., and Hornung, H. G., "Differential Interferometric Measurement of Instability at Two Points in a Hypervelocity Boundary Layer," *Proceedings of 51st AIAA Aerospace Sciences Meeting Including the New Horizons Forum and Aerospace Exposition*, AIAA-2013-0521, Grapevine, Texas, 2013. https://doi.org/10.2514/6.2013-521.

[22] Parziale, N. J., Shepherd, J. E., and Hornung, H. G., "Differential Interferometric Measurement of Instability in a Hypervelocity Boundary Layer," *AIAA Journal*, Vol. 51, No. 3, 2013, pp. 750–754. https://doi.org/10.2514/1.J052013.

[23] Parziale, N. J., "Slender-Body Hypervelocity Boundary-Layer Instability," Ph.D. thesis, California Institute of Technology, 2013.

[24] Parziale, N. J., Shepherd, J. E., and Hornung, H. G., "Free-stream density perturbations in a reflected-shock tunnel," *Experiments in Fluids*, Vol. 55, No. 2, 2014, p. 1665. https://doi.org/10.1007/s00348-014-1665-0.

[25] Parziale, N. J., Shepherd, J. E., and Hornung, H. G., "Observations of hypervelocity boundary-layer instability," *Journal of Fluid Mechanics*, Vol. 781, 2015, pp. 87–112. https://doi.org/10.1017/jfm.2015.489.

[26] Jewell, J. S., Parziale, N. J., Lam, K.-L., Hagen, B. J., and Kimmel, R. L., "Disturbance and Phase Speed Measurements for Shock Tubes and Hypersonic Boundary-Layer Instability," *Proceedings of 32nd AIAA Aerodynamic Measurement Technology and Ground Testing Conference*, AIAA-2016-3112, Washington, D. C., 2016. https://doi.org/10.2514/6.2016-3112.

[27] Jewell, J. S., Hameed, A., Parziale, N. J., and Gogineni, S. P., "Disturbance Speed Measurements in a Circular Jet via Double Focused Laser Differential Interferometry," *Proceedings of AIAA Scitech 2019*, AIAA-2019-2293, San Diego, California, 2019. https://doi.org/10.2514/6.2019-2293.

[28] Ceruzzi, A. P., and Cadou, C. P., "Simultaneous Velocity and Density Gradient Measurements using Two-Point Focused Laser Differential Interferometry," *Proceedings of AIAA Scitech 2019*, AIAA-2019-2295, San Diego, California, 2019. https://doi.org/10.2514/6.2019-2295.

[29] Ceruzzi, A. P., Callis, B., Weber, D., and Cadou, C. P., "Application of Focused Laser Differential Interferometry (FLDI) in a Supersonic Boundary Layer," *Proceedings of AIAA Scitech 2020*, AIAA-2020-1973, Orlando, Florida, 2020. https://doi.org/10.2514/6.2020-1973.

[30] Weisberger, J. M., Bathel, B. F., Herring, G. C., King, R. A., Chou, A., and Jones, S. B., "Focused Laser Differential Interferometry Measurements at NASA Langley 20-Inch Mach 6," *Proceedings of AIAA Aviation Forum*, AIAA-2019-2903, Dallas, Texas, 2019. https://doi.org/10.2514/6.2019-2903.

[31] Bathel, B. F., Weisberger, J. M., Herring, G. C., King, R. A., Jones, S. B., Kennedy, R. E., and Laurence, S. J., "Two-point, parallel-beam focused laser differential interferometry with a Nomarski prism," *Applied Optics*, Vol. 59, No. 2, 2020, pp. 244–252. https://doi.org/10.1364/AO.59.000244.

[32] Price, T. J., Gragston, M., Schmisseur, J. D., and Kreth, P. A., "Measurement of supersonic jet screech with focused laser differential interferometry," *Applied Optics*, Vol. 59, No. 28, 2020, pp. 8902–8908. https://doi.org/10.1364/AO.402011.

[33] Hameed, A., Parziale, N. J., Paquin, L., Butler, C., and Laurence, S. J., "Hypersonic Slender-Cone Boundary Layer Instability in the UMD HyperTERP Shock Tunnel," *Proceedings of AIAA SciTech 2020*, AIAA-2020-0362, Orlando, Florida, 2020, pp. 1–14. https://doi.org/10.2514/6.2020-0362.

[34] Harris, A. J., Kreth, P. A., Combs, C. S., and Schmisseur, J. D., "Laser Differential Interferometry and Schlieren as an Approach to Characterizing Freestream Disturbance Levels," *2018 AIAA Aerospace Sciences Meeting*, AIAA 2018-1100, Kissimmee, Florida, 2018. https://doi.org/10.2514/6.2018-1100.

[35] Lawson, J. M., and Austin, J. M., "Expansion Tube Freestream Disturbance Measurements using a Focused Laser Differential Interferometer," *Proceedings of AIAA Scitech 2020*, AIAA-2020-1064, Orlando, Florida, 2020. https://doi.org/10.2514/6.2020-1064.

[36] Birch, B., Buttsworth, D., and Zander, F., "Measurements of freestream density fluctuations in a hypersonic wind tunnel," *Experiments in Fluids*, Vol. 61, No. 7, 2020, pp. 1–13. https://doi.org/10.1007/s00348-020-02992-w.

[37] Hedlund, B., Houpt, A., Gordeyev, S., and Leonov, S., "Measurement of Flow Perturbation Spectra in Mach 4.5 Corner Separation Zone," *AIAA Journal*, Vol. 56, No. 7, 2018, pp. 2699–2711. https://doi.org/10.2514/1.J056576.

[38] Houpt, A. W., and Leonov, S. B., "Focused Laser Differential Interferometer for Supersonic Boundary Layer Measurements on Flat Plate Geometries," *Proceedings of the 2018 Plasmadynamics and Lasers Conference*, AIAA-2018-3434, Atlanta, Georgia, 2018. https://doi.org/10.2514/6.2018-3434.

[39] Houpt, A. W., and Leonov, S. B., "Focused and Cylindrical-Focused Laser Differential Interferometer Characterization of SBR-50 at Mach 2," *Proceedings of AIAA Aviation 2019*, AIAA-2019-3383, Dallas, Texas, 2019. https://doi.org/10.2514/6.2019-3383.

[40] Benitez, E. K., Jewell, J. S., and Schneider, S. P., "Focused Laser Differential Interferometry for Hypersonic Flow Instability Measurements with Contoured Tunnel Windows," *Proceedings of AIAA Scitech 2020*, AIAA-2020-1282, Orlando, Florida, 2020. https://doi.org/10.2514/6.2020-1282.

[41] Benitez, E. K., Esquieu, S., Jewell, J. S., and Schneider, S. P., "Instability Measurements on an Axisymmetric Separation Bubble at Mach 6," *Proceedings of AIAA Aviation 2020*, AIAA-2020-3072, Virtual Event, 2020. https://doi.org/10.2514/6.2020-3072.

[42] Ramprakash, A., McIntyre, T. J., Wheatley, V., and Mee, D. J., "Performance Analysis of FLDI Technique using Turbulent Jets," *Proceedings of the IX Australian Conference on Laser Diagnostics*, Adelaide, Australia, 2019.

[43] Lawson, J. M., Neet, M. C., Grossman, I. J., and Austin, J. M., "Characterization of a Focused Laser Differential Interferometer," *Proceedings of AIAA Scitech 2019*, AIAA-2019-2296, San Diego, California, 2019. https://doi.org/10.2514/6.2019-2296.

[44] Lawson, J. M., Neet, M. C., Grossman, I. J., and Austin, J. M., "Static and dynamic characterization of a focused laser differential interferometer," *Experiments in Fluids*, Vol. 61, No. 8, 2020, pp. 1–11. https://doi.org/10.1007/s00348-020-03013-6.

[45] Fulghum, M. R., "Turbulence measurements in high-speed wind tunnels using focusing laser differential interferometry," Ph.D. thesis, The Pennsylvania State University, 2014.

[46] Settles, G. S., and Fulghum, M. R., "The Focusing Laser Differential Interferometer, an Instrument for Localized Turbulence Measurements in Refractive Flows," *Journal of Fluids Engineering*, Vol. 138, No. 10, 2016, p. 101402. https://doi.org/10.1115/1.4033960.

[47] Schmidt, B. E., and Shepherd, J. E., "Analysis of focused laser differential interferometry," *Applied Optics*, Vol. 54, No. 28, 2015, pp. 8459–8472. https://doi.org/10.1364/AO.54.008459.

[48] Hornung, H. G., "Performance Data of the New Free-Piston Shock Tunnel at GALCIT," *Proceedings of 17th AIAA Aerospace Ground Testing Conference*, AIAA 1992-3943, Nashville, TN, 1992. https://doi.org/10.2514/6.1992-3943.

[49] Goodwin, D. G., "An Open-Source, Extensible Software Suite for CVD Process Simulation," *Proceedings of CVD XVI and EuroCVD Fourteen, M Allendorf, F Maury, and F Teyssandier (Eds.)*, 2003, pp. 155–162.

[50] Browne, S., Ziegler, J., and Shepherd, J. E., "Numerical Solution Methods for Shock and Detonation Jump Conditions," GALCIT - FM2006-006, 2006.

[51] Wright, M. J., Candler, G. V., and Prampolini, M., "Data-parallel Lower-upper Relaxation Method for the Navier-Stokes Equations," *AIAA Journal*, Vol. 34, No. 7, 1996, pp. 1371–1377. https://doi.org/10.2514/3.13242.

[52] Candler, G. V., "Hypersonic Nozzle Analysis Using an Excluded Volume Equation of State," *Proceedings of 38th AIAA Thermophysics Conference*, AIAA-2005-5202, Toronto, Ontario Canada, 2005. https://doi.org/10.2514/6.2005-5202.

[53] Johnson, H. B., "Thermochemical Interactions in Hypersonic Boundary Layer Stabity," Ph.D. thesis, University of Minnesota, Minneapolis , Minnesota, 2000.

[54] Wagnild, R. M., "High Enthalpy Effects on Two Boundary Layer Disturbances in Supersonic and Hypersonic Flow," Ph.D. thesis, University of Minnesota, Minnesota, 2012.

[55] Gragston, M., Siddiqui, F., and Schmisseur, J. D., "Detection of second-mode instabilities on a flared cone in Mach 6 quiet flow with linear array focused laser differential interferometry," *Experiments in Fluids*, Vol. 62, No. 81, 2021. https://doi.org/10.1007/s00348-021-03188-6.

[56] Gragston, M., Price, T. J., Davenport, K., Zhang, Z., and Schmisseur, J. D., "Linear array focused-laser differential interferometry for single-shot multi-point flow disturbance measurements," *Optics Letters*, Vol. 46, No. 1, 2021, pp. 154–157. https://doi.org/10.1364/OL.412495.

[57] Hameed, A., and Parziale, N. J., "Focused Laser Differential Interferometry Transfer Functions for Complex Density Disturbance Fields," *Proceedings of AIAA Aviation Forum 2021*, AIAA-2021-2907, Virtual Event, 2021. https://doi.org/10.2514/6.2021-2907.

[58] Johnson, H. B., Seipp, T. G., and Candler, G. V., "Numerical Study of Hypersonic Reacting Boundary Layer Transition on Cones," *Physics of Fluids*, Vol. 10, No. 13, 1998, pp. 2676–2685. https://doi.org/10.1063/1.869781.

[59] Paquin, L. A., Skinner, S. N., Laurence, S. J., Hameed, A., Shekhtman, D., Parziale, N., Yu, W. M., and Austin, J. M., "Hypersonic Boundary-Layer Instability on a Highly Cooled Cone. Part II: Schlieren Analysis of Boundary-Layer Disturbances," *Proceedings of AIAA Scitech 2022*, AIAA-2022, Virtual Event, 2022.

[60] Shekhtman, D., Mustafa, M. A., Parziale, N. J., Yu, W. M., and Austin, J. M., "Krypton Tagging Velocimetry (KTV) Investigation in the Caltech T5 Reflected-Shock Tunnel," *Proceedings of AIAA SciTech 2021*, AIAA-2021-1302, Virtual Event, 2021. https://doi.org/10.2514/6.2021-1302.

[61] Shekhtman, D., Yu, W. M., Mustafa, M. A., Parziale, N. J., and Austin, J. M., "Freestream velocity-profile measurement in a large-scale, high-enthalpy reflected-shock tunnel," *Experiments in Fluids*, Vol. 62, No. 118, 2021, pp. 1–13. https://doi.org/10.1007/s00348-021-03207-6.

[62] Girard, J., Finch, P. M., Schwartz, T., Yu, W., Strand, C. L., Austin, J. M., Hornung, H. G., and Hanson, R. K., "Characterization of the T5 Reflected Shock Tunnel Freestream Temperature, Velocity, and Composition using Laser Absorption Spectroscopy," *AIAA Propulsion and Energy 2021 Forum*, AIAA-2021-3525, Virtual Event, 2021. https://doi.org/10.2514/6.2021-3525.